INSTITUTE OF COMPUTER SCIENCES
Master in Artificial Intelligence and Data Science

Universitätsstr. 1 D–40225 Düsseldorf

Heinrich Heine Universität Düsseldorf

AI-based fluorescent labeling for cell line development

Hanna Pankova

Master thesis

Date of issue: 01. April 2022
Date of submission: 29. August 2022
Reviewers: Prof. Dr. Markus Kollmann
Dr. Wolfgang Halter

Erklärung

Hiermit versichere ich, dass ich diese Master thesis selbstständig verfasst habe. Ich habe dazu keine anderen als die angegebenen Quellen und Hilfsmittel verwendet.

Düsseldorf, den 29. August 2022

Hanna Pankova

Abstract

Cell line development is an expensive and time-consuming process, however that is the most modern approach for producing the proteins needed in various pharmaceuticals.

Contents

1 Introduction

1.1 Motivation

Nowadays recombinant proteins are widely used in biomedical research and production of medicines that are used in the variety of therapeutic neeeds like vaccines and antibodies [TODO add references]. Therefore there is currently a great need for high-volume and high-quality recombinant protein production. That is why the optimization and improvement of cell line development (CLD) as a process in use for the production of recombinant proteins is extremely important.

Clone screening is a step of the CLD process in which cells are analyzed for further selection of the most stable and productive clones. Fluorescence microscopy provides data about the cell structure that enables better clone selection, however it is not only expensive and time-consuming, but also toxic for the cells. Automating fluorescence microscopy for clone selection via convolutional neural networks *in silico* significantly simplifies the existing procedure of clone selection, reducing phototoxicity, time and expenses needed for the analysis.

The goal of this thesis is to provide a proof of concept on whether an *in silico* approach to fluorescent labeling can substitute manual cell staining and provide all the needed information that would be used for further clone screening and selection. That is particularly why the research at hand is aimed towards the specific needs, pipelines and data used at Merck KgaA. In this research four UNet models (for four target proteins highlighting different cell organelles) were developed for automating fluorescence cell staining based on DIC microscopy imaging of CHO cells: nuclei, endoplasmic reticulum, [[green fluorescent protein]] and Golgi apparatus. Another important goal of this research that differentiates it from the similar studies like [TODO cite LaChance 2020 and cite Christiansen 2018] is to not only provide deep learning models for the fluorescence predictions but also study their reliability and be able to detect drift during image acquisition that can happen quite easily due to the sensitivity of the microscope settings as well as the cell phenotypes, scaling and fixation procedures.

This thesis is laid out as follows: Section 2 reviews the biological concepts needed to understand the application of this research, it also reviews machine and deep learning concepts used for data analysis; Section 3 provides an overview of the implementation and the results of the experimental *in silico* fluorescence predictions; Section 4 shows stability of the deep learning models developed in the previous section and provides valuable insights on the information from their embeddings; Section 5 details the practical tools used for the development at Merck KgaA and Section 6 explores possible future research questions that arose from the current analysis and provides concluding remarks and succinct recommendations.

1.2 Notation

$\boldsymbol{x}^{(i)}$	The i-th input image (sample) from a dataset
$\boldsymbol{X}_{train}$	A set of training examples
$\boldsymbol{y}^{(i)}$	The target image associated with the i-th input sample from a dataset
$\mathbb{R}$	A set of real numbers
$A_{i,j}$	An element on the i-th row and j-th column of a matrix A
p_{data}	Data generating distribution

2 Domain knowledge

The *in silico* fluorescence labeling approach has proven to be very promising as a substitute to the manual cell staining processes [TODO cite all the relevant references]. For example, the research of [TODO cite Christiansen 2018] did not only prove successful prediction of different cell stains with a variety of modalities and cell types, but it had also successfully determined cell viability. Nevertheless, the study is limited mainly to transmitted light (TL) z-stack imaging. This refers to the networks input being comprised of 3D images, which is not the case in this work. [cite Ounkomol 2018] too shows succeful predictions of several organelles in bright-field TL 3D images using 3D convolutional neural networks. However, switching to 2D data did not yield adequate results for them. Other, newer studies like [cite Ugawa 2021] provide an application of label-free fluorescence predicting already at the sorting stage, when a high-throughput system sorts cells individually. However, only a single-pixel detector is used by this study, meaning that it captures a wave rather than an image. Nonetheless one can recover an image with heavy computations if needed [cite Sadao Ota 2018].

There are two very promising studies by [cite Cheng 2021] and [cite LaChance 2020]. Even though the former manages to reach a state-of-the art performance on label-free fluorescence reconstruction, it uses reflectance images from oblique dark-field illumination as the input, which is a more specific cell imaging approach. Still, this input provides higher structural contrast in comparison to any transmission technique [cite Boustany 2010]. The latter study uses an easier imaging technique (DIC imaging) as an input, which shows great results even with low-resolution data. Both of these studies provide results based not only on training metrics, but also on performance of the models for metrics used in the downstream tasks. This is very important in the label-free fluorescence labeling research and was not present in papers before LaChance. In the thesis at hand, many methods from the LaChance paper were used as both the data and the processes in the project pipeline of Merck KgaA align very well with the study conducted in that paper.

All of the studies mentioned above, as well as this work rely on the premise that the input imaging type (here DIC) contains enough information to predict the fluorescence signal from it. This is a reasonable assumption because DIC, as well as bright-field and phase contrast imaging, are very often used for determining cell morphology [TODO cite Kasprowicz 2017].

This chapter provides a brief overview of the biological background needed to understand the process of cell line development (CLD) and the role of fluorescent *in silico* labeling of DIC cell images within. It also covers the fundamentals of deep and machine learning techniques used here including clustering and dimensionality reduction approaches. At the end of the chapter, a brief summary of the microscopy image acquisition process used in the research is given.

2.1 Biology

2.1.1 Cell line development process

Cell line development (CLD) is a process of generating single cell-derived clones that produce high and consistent levels of target therapeutic protein [TODO cite pharma.lonza.com/offerings/mammalian/cell-line-development]. Therapeutic proteins in this case are so-called recombinant proteins and they are widely used in the biomedical research, drug production and for various therapeutic needs like, for example, vaccines and monoclonal antibodies (mAbs) **IWNLP**$^{\textbf{iqbal2007underwater}}$ [TODO cite Ohtake 2013, Jefferis 2021, Funaro 1996]. A recombinant protein is defined by [cite Barbeau, J] is a modified or manipulated protein encoded by a recombinant DNA. Recombinant DNA, in its turn, consists of a plasmid, where the genes of the target protein of interest are cloned downstream of a promoter region. As soon as this plasmid will be transfected to a host cell (for example some mammalian cells that are able to produce the protein), the host will start to express this protein of interest. Today, in both industry and research there is a great need for production of high volumes of good-quality recombinant proteins [TODO cite Tihanyi 2020]. That is why the goal of many research efforts in recombinant protein production is to improve expression efficiency and create high-throughput systems to improve the CLD processes [cite Tihanyi 2020].

One of the most popular host cells used in CLD and in this work specifically are chinese hamster ovary (CHO) cells [cite Castan 2018]. Altough different cells can be used as hosts, such as bacterial, plant-based or yeast cells, mammalian cells remain the most popular [cite Beckman]. The reason behind this popularity hides in the fact that they can produce a diverse range of correctly folded proteins and most importantly, they have high protein production rates. Productivity rate is measured in titre of produced protein, and CHO cells can reach 0.1 - 1 g/L in batch and 1-10 g/L in fed-batch [TODO add reference] cultures [cite Tihanyi 2020]. Mostly all of the mAbs are produced using CHO cells [cite Lalonde 2017]. Companies mostly use the same host cell line for all their productions because already checked and qualified cells simplify the road to the clinic [cite Tihanyi 2020]. That is why current research has a wide applicability.

However there is a downside to using CHO as host cells - they are infamously unstable. As rapidly growing immortal cells CHO are also genomically unstable and extremely heterogeous which ususally leads to the main issue: production instability. The problem of choosing stable and high-production clones that simutaneously will be able to express protein qualitatively and quantifiably over time is essentially the main goal of current research. The big challenge in manufacturing here is the time and the costs of production. Currently, a lot of research attention is dedicated to the reduction of both, as well as to developing techniques of high-throughput clone screening and characterization [cite Tihanyi 2020]. The latter is of interest for this thesis. With the great amounts of data acquired over time and the development of the computational modelling and statistical analysis it is possible now to do the analysis *in silico*, meaning - computationally without interferring with the cells instead of the usual *in vitro* analysis.

2.1.1.1 CLD steps

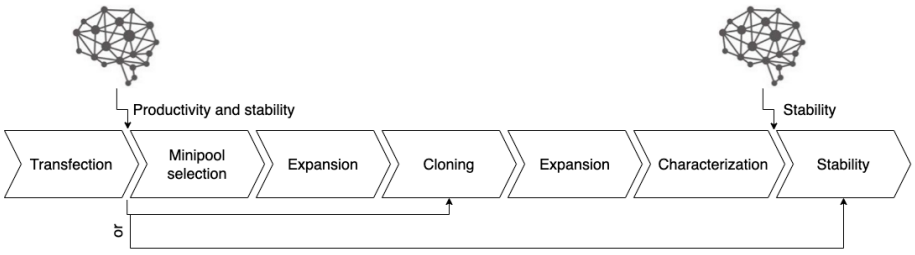

Figure 1: CLD process steps

The first step of CLD is called transfection - the introduction of the gene of interest (GOI or a DNA vector or alternatively an expression vector) into CHO cells. It has two main problems: first is that transfection mostly results in a vector being inserted into a random site within the host cell genome and second, that it generally has low efficiency of integration [cite Tihanyi]. It is important to transfect a GOI into the optimal site of the genome to secure high protein expression over time during protein production, however practically, transfection happens into a random location of genome. In cases where the gene was transfected into an inactive site of genome (essentially the majority of genome is transcriptionally inactive), the cell will likely be unable to express the gene [cite Castan, Hong 2018].

The second step of the process is selection of cell minipools that have successful and stable gene integrations for further expansion and cloning. The reason for not all of them being suitable is that during the transfection step, only 80% of the cells will receive a GOI vector [cite Castan]. Only a small percent of these cells actually integrate a vector into the genome and, as mentioned above, only a fraction of those are able to stably express the protein [a better reference needed Shin 2020]. After the best minipools are selected, they will be expanded.

The third step in CLD is to clone the cells. Chosen stable pools of cells are phenotypically and genetically diverse - meaning they have different growth rates, metabolic profile and etc. This is not ideal for industrial production - all the cells used for protein production should be derived from the same clone [cite [25] from Castan].

Once the cells are cloned, phenotypical and genetical heterogeneity is reduced, the next step is to characterize the cells for their expression of the GOI. One has to estimate the clones' productivity and stability. Such observations may take up to 90 days (usually the checks are made on the 30th, 60th and 90th days). If the clones remain stable after this time and are able to express enough of the protein, then they are suitable for further production. However this last step costs a lot of time and maintenance costs for feeding and analysing the cells. Predicting productivity and stability of the cells on ealier stages would reduce this time significantly or even allow to avoid this process completely.

2.1.2 Project specifications of cell line development for Merck KgaA

There are many different proteins that can be produced using such technologies, for example, vaccines, hormones, sugars etc., however this research is dedicated to the production of monoclonal antibodies (mAbs).

CHOZN® Platform is a currently widely used product of Merk KgaA. CHOZN is a CHO mammalian cell expression system for fast and easy selection and growth of clones producing high levels of recombinant proteins [cite tech-bulletin]. The processes of developing expression systems on this platform correspond to the general CLD process described in the previous subsection [put subsection number]. The scope of the project is to simplify the labour-intensive and time-consuming process of stability measurement of the expression system by inducing predictions of productivity and stability rates during early steps in the CLD process.

After the transfection step there are several quantities that are measured in minipools in order to select the best ones. For example, cell size, its complexity, cell surface protein expression, endoplasmic reticulum (ER) mass, mitochondria mass, etc. For qualitative and quantitative characterization of cells, fluorescent labeling is used. It is a process of covalently binding fluorescent dyes to biomolecules such as nucleic acids or proteins, so that they can be visualized via fluorescence imaging [cite https://www.nature.com/subjects/fluorescent-labelling]. A fluorophore is a chemical compound that can reemit light at a certain wavelength.These compounds are a critical tool in biology because they allow experimentators to capture particular components of a given cell in detail [cite O'reilly life sciences p113].

Unfortunately, fluorescence labeling is expensive, time-consuming and may kill the cell due to its phototoxicity [cite Fried et al., 1982; Patil et al., 2018; Progatzky et al., 2013)]. Additionally, Yeo et al. [cite Tihanyi] found out that different selection markers affect the production stability of CHO cells. Other negative aspects of manual staining appoach are: there is a limited number of available fluorescent channels in microscopes; some fluorophores have a spectral overlap, hence there is a limited number of detectable markers [cite Perfetto et al., 2004]; such labels can be inconsistent [cite Burry, 2011; Weigert et al., 1970), and depend a lot on reagent quality and require many hours of lab work. Toxicity, for instance, is a very dangerous factor, especially for medicine production as it may even affect the final product. Therefore there exists a need for an approach of *in silico* flurescent labeling - computationally and without affecting the cell.

For *in silico* labeling, the input data is a differential interference contrast (DIC) microscopy. This is an optical microscopy technique used to enhance the contrast in unstained, transparent samples [cite wikipedia?]. This is a much cheaper image acquision technique than a staining process, and it has much less variability as well (for example, no dependency on the dye or antibody quality). The research is dedicated to predicting fluorescence signal from the DIC imaging directly without the need of actual cell staining. The measurements needed for selection of minipools can be calculated as usual, but using the predicted images instead.

2.2 Deep learning and machine learning basics

2.2.1 Neural networks

Definition 2.1 (Image dataset)**.** An image dataset in current thesis constists of input DIC images X and target fluroescence images Y. Together pairs from each form a dataset:

$$D = (X, Y) = \{(x^{(1)}, y^{(1)}), \dots, (x^{(N)}, y^{(N)})\} \tag{1}$$

where both $x^{(i)}$ and $y^{(i)} \in \mathbb{R}^{W \times H}$ are single images, N is the size of the dataset. Generally input data has a shape of (N, C, H, W), in this work $C = 1$.

Definition 2.2 (Model)**.** A model is a function with learnable parameters $\theta = (\theta_1, ..., \theta_K)$ where $\theta_i \in \mathbb{R}$ for $i \in 0, ..., K$ which approximates the mapping of initial data X to target data Y.

$$M(X, \theta) = Y' \approx Y \tag{2}$$

Definition 2.3 (Loss function)**.** Loss function is a function $L(y, M(x, \theta))$ of model's parameters θ, that for $(x^{(i)}, y^{(i)}) \in D$ outputs a scalar value measuring the difference between ground truth y and prediction $M(x, \theta)$. Usually loss function can be written as an average over the training set:

$$J(\theta) = \mathbb{E}_{(x,y)\sim p_{data}} L(y, M(x, \theta)) \tag{3}$$

where p_{data} denotes an empirical distribution of the training data.

Definition 2.4 (Binary-cross entropy loss)**.** Let $y \in \mathbb{R}^{W \times H}$ be a ground truth image and $y' \in \mathbb{R}^{W \times H}$ be a prediction. Binary-cross entropy loss is defined as:

$$L(y, y') = -\frac{1}{N^2} \sum_{i=1}^{H} \sum_{j=1}^{W} y_{i,j} \cdot \log\big(y'_{i,j}\big) + (1 - y_{i,j}) \cdot \log\big(1 - y'_{i,j}\big) \tag{4}$$

Definition 2.5 (MSE (mean squared error) loss)**.** Let $y \in \mathbb{R}^{W \times H}$ be the ground truth and $y' \in \mathbb{R}^{W \times H}$ be the predicted images. The MSE loss is defined as:

$$L(y, y') = \sum_{i=1}^{H} \sum_{j=1}^{W} (y_{i,j} - y'_{i,j})^2 \tag{5}$$

Definition 2.6 (PCC (Pearson correlation coefficient) loss)**.** Let $y \in \mathbb{R}^{WH}$ be a flattened ground truth and $y' \in \mathbb{R}^{WH}$ be a flattened predicted image. The PCC loss is defined as:

$$L(y, y') = \frac{\sum_{i=1}^{WH} (y_i - \bar{y})(y'_i - \bar{y}')}{\sqrt{\sum_{i=1}^{WH^2} (y_i - \bar{y})^2 (y'_i - \bar{y}')^2}} \tag{6}$$

where $\bar{y}$, $\bar{y}'$ are means of the ground truth and predicted images respectively.

This loss is spreadly used in cell biology for comparison of co-localization between the proteins. PCC is also popular in computer vision where it is used there for determining image similarity in terms of spatial-intensity [cite Cohen].

Definition 2.7 (Optimization)**.** Optimizer is a process of updating the parameters θ of the model $M(X, \theta)$ to minimize the loss function $L(y, M(x, \theta))$.

With maximum likelihood estimation one has that:

$$\theta_{MLE} = \arg\max_{\theta} \sum_{i=1}^{N} \log p_{\text{model}}(x^{(i)}, y^{(i)}, \theta) \tag{7}$$

After maximizing the sum and taking a gradient one gets:

$$\nabla_\theta J(\theta) = \mathbb{E}_{x,y\sim p_{data}} \nabla_\theta \log p_{\text{model}}(x, y, \theta) \tag{8}$$

The exact gradient then on a discetized data-generting distribution is:

$$g = \nabla_\theta J^*(\theta) = \sum_x \sum_y p_{\text{data}}(x, y) \nabla_\theta L(y, M(x, \theta)) \tag{9}$$

Here one can obtain an unbiased estimator of a true gradient on a minibatch of i.i.d. samples $\{x^{(i)}, ..., x^{(m)}\}$

$$\hat{g} = \frac{1}{m} \nabla_\theta \sum_i L(y^{(i)}, M(x^{(i)}, \theta)) \tag{10}$$

Definition 2.8 (Stohastic gradient descent)**.** Stohastic gradient descent is an optimization algorithm where the parameters θ are iteratively updated every mini-batch of data by the following rule:

$$\theta_{k+1} = \theta_k - \alpha \frac{1}{m} \nabla_\theta \sum_i L(y^{(i)}, M(x^{(i)}, \theta)) \tag{11}$$

where α is a tuneable parameter called *learning rate*.

Definition 2.9 (Adadelta optimizer)**.** Adadelta optimizer is a more sophisticated optimization technique, that follows the following algorithm for the parameters update: Stohastic

Algorithm 1 Adadelta optimization

1. $E[g]_0^2 = 0$ and $E[\Delta\theta^2]_0 = 0$ In order to update the parameters compute:
2. Compute gradient: $\hat{g}_t$
3. Accumulate gradient: $E[g]_t^2 = \rho E[g]_{t-1}^2 + (1-\rho) g_t^2$
4. Compute update: $\Delta\theta_t = \frac{\text{RMS}[\Delta\theta]_{t-1}}{\text{RMS}[g]_t} \hat{g}_t$
5. Accumulate updates: $E[\Delta\theta^2]_t = \rho E[\Delta\theta^2]_{t-1} + (1-\rho)\Delta\theta_t^2$
6. Apply update: $\theta_{t+1} = \theta_t + \Delta\theta_t$

RMS here is the root mean square. [cite Zeiler 2012]

gradient descent is an optimization algorithm where the parameters θ are iteratively updated every mini-batch of data by the following rule:

$$\theta_{k+1} = \theta_k - \alpha \frac{1}{m} \nabla_\theta \sum_i L(y^{(i)}, M(x^{(i)}, \theta)) \tag{12}$$

where α is a tuneable parameter called *learning rate*.

Definition 2.10 (Feedforward fully-connected layer)**.** A feedforward fully-connected layer is a trainable function with parameters $W \in \mathbb{R}^{N \times M}$ (weights) and $b \in \mathbb{R}^M$ (biases) that maps in this case a vector $x \in \mathbb{R}^N$ to an output $a \in \mathbb{R}^M$ via the following transformation:

$$a = W^T x + b \tag{13}$$

This is one of the simplest layers in a feedforward neural networks and input and output in it as mentioned above are vectors. However in this study inputs and outputs are images, that are represented in memory as square matrices $x^{(i)}, y^{(i)} \in \mathbb{R}^{W \times H}$. One could simply flatten the image into a vector and use it as an input to a fully-connected feedforward neural network, nevertheless this would be a suboptimal approach.

Since essentially one of the main tasks of this research is to create a deep learning model that is able to predict a fluorescence image from a DIC image, the problem statement could be boiled down to the following: predict an intensity high-resolution image from another intensity high-resolution image based on the features of the object morphology in it. Such problem is very common in the field of image analysis and one of the popular deep learning tools for solving such problems is convolutional neural network (CNN) or more specifially a UNet.

CNNs are able to capture nonlinear relationships over large areas of images, they greatly improve performance for image recognition tasks in comparison to classical machine learning methods [TODO cite Oukomol]. The word "convolutional" in its name suggests that the convolution operation should be used in at least one of the layers there.

Definition 2.11 (Convolutional layer)**.** A convolutional layer is a trainable function with parametrized kernel $K \in \mathbb{R}^{F \times F \times C}$ and bias $b \in \mathbb{R}$ that is usually denoted via operator $(\cdot * \cdot)$. By transforming an input $x \in \mathbb{R}^{W,H,C}$ it produces an output S

$$S = K * x + b \tag{14}$$

that is called a *feature map* where an element on position (i, j) is defined as follows:

$$S_{i,j} = \sum_w \sum_h x_{m,n} K_{i-m,j-n} \tag{15}$$

Convolutional layer like a fully-connected layer can be viewed a linear transformation as well. However there are 3 main advantages that leverage convolutional layers for image processing in comparison to fully-connected layers: sparse interations, parameter sharing, equivariant representations. Image is a very redundant way of representing the semantic meaning hidden in it. Having a value of one pixel, the probability that the neighboring one will be of the same color is very high. Sparsity of interactions can be described by an example: usually a high-resolution image might have millions pixels, however it is possible to detect smaller and very important features like contrast changes, edges, and shapes using a kernel consisting only of a hundred of pixels. By applying kernels (or filters) on the image locally one will infer many of these features across the whole image. Such approach reduces the memory needed for parameter storing and improves its statistical

efficiency [cite DL-book]. Parameter sharing refers to the fact that instead of learning a separate set of parameters for every location within the image, will be learned only one set of the parameters and applied across all image locations. Lastly, equivariance here means that convolution operation is equivarient to the shifts in the image.

Definition 2.12 (Stride)**.** During the computation of convolution, kernel starts sliding at the upper-left corner of the input tensor, all over all locations to the right and down. The step with which the window slides is called *stride*.

Definition 2.13 (Padding)**.** When convolution is applied several points on the perimeter of the input tensor will be lost. One can fix this by adding few more pixels of the perimeter, to preserve the dimension of the output same as input. The amout of pixels addded is called *padding*.

Definition 2.14 (Max-pooling layer)**.** Maximum pooling operation reports the maximum output within a rectangular neighborhood [cite DL-book].

Since adding two linear functions together would produce a linear function, it is important to use activation functions (or non-linearities) after each convolutional or linear layer like RELU, ELU, Tahn, Sigmoids and etc. In CNNs they are also often combined with max pooling layers and dropouts to escape overfitting.

Definition 2.15 (Batch normalization layer)**.** Let's denote $B = \{x^{(i)}, ..., x^{(m)}\}$ to be a mini-batch of data. Then Batch Normalizing transform applied to this input data would be:

$$\begin{aligned} a^{(i)} &= \gamma \frac{x^{(i)} - \mu_B}{\sigma_B^2 + \epsilon} + \beta \\ \sigma_B^2 &= \frac{1}{m} \sum_i^m (x^{(i)} - \mu_B)^2 \\ \mu_B &= \frac{1}{m} \sum_i^m x^{(i)} \end{aligned} \tag{16}$$

where γ and β are learnable parameters, μ_B and σ_B^2 are the mean and standard deviation of the batch. [cite Ioffe and Szegedy, 2015]

Definition 2.16 (Dropout layer)**.** Dropout is a technique that randomly sets some weights (units) to zero [cite Srivastava, Hinton 2014]. It leads to the training of several smaller networks that share the parameters. If a mask vector μ specifies which units are included in training, then dropout's objective to be minimized becomes: $\mathbb{E}_\mu J(\theta, \mu)$. Visually dropout is presented in the Figure 2.

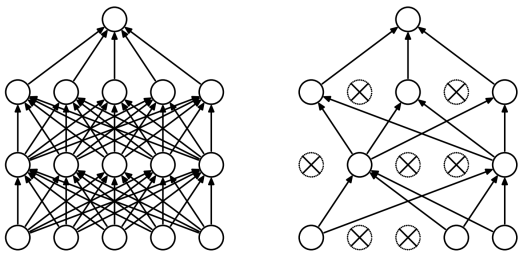

Figure 2: Dropout

Definition 2.17 (Activation function)**.** An activation function is an element-wise non-linear function $f(\cdot)$. Some examples with are:

$$f(x) = \frac{1}{1+e^{-x}} \quad \text{Sigmoid} \tag{17}$$

$$f(x) = max(0, x) \quad \text{Rectified linear unit (ReLU)} \tag{18}$$

$$f(x) = \begin{cases} x, & \text{if } x > 0 \\ \alpha * (e^x - 1), & \text{if } x \leq 0 \end{cases} \quad \text{ELU} \tag{19}$$

Models in this work mostly use ELU activations as ELU provides a better signal flow between the layers by not cutting off the negative values completely.

Definition 2.18 (UNet)**.** UNet is fully convolutional neural network wiht U-shaped encoder-decoder network architecture. [cite Ronneberger].

The encoder is a usual CNN, consisting of the repeated block of two 3×3 convolutions, followed by an activation function, and a 2×2 max-pooling operation with stride 2. At each ecnoder step the number of feature channels doubles. The decoder is also a usual CNN, consisting of repeated blocks of transposed convolution, that halves the number of feature channels, followed by a concatenation with a corresponding output from an encoder, and two 3×3 convolutions, followed by a ReLU. The last decoder layer is a 1×1 convolution to map the tensor to the number of output image channels need. Skip-connections is a very important part of UNet as they allow to the flow of high-resolution features from the encoder to the decoder that in turn allows to restore a corresponding high-resolution image.

Definition 2.19 (Autoencoder)**.** Autoencoder is an unsupervised learning technique in neural networks for the representation learning purposes. Autoencoder consists of an encoder that compresses data into a lower dimensional representationa and a decoder that restores the original input from the encoded representation.

Definition 2.20 (Overfitting)**.** "Hypothesis overfits the training samples if some other hypothesis that fits the training samples less well actually performs better over the entire distribution of instances" (cite p67 Mitchell Machine Learning 1997). They way to avoid overfitting that happened to the models in Sections [TODO cite sections] are discussed in Section [cite regularization section].

2.2.2 Dimensionality reduction methods

This reseach additionally provides the study of the embeddings of a trained UNet and an Autoencoder in Chapter [TODO cite chapter]. In order to understand the visualizations better all dimensionality reduction methods that were used here are listed and explained in this subsection.

Definition 2.21 (Embedding)**.** An embedding in this context is an output tensor from the encoder part of the UNet or from an encoder part of an Autoencoder.

The encoder output of the UNet is a tensor of size $16 \times 16 \times 256$ and after its flattening it turns into a vector of size 655536. The smallest autoencoder embedding was of size 200 [TODO check] which is also high-dimensional. One of the tasks of this research if to determine wethere there are any interesting patterns or grouping based of various criteria hidden within the bottleneck embeddings, and wether they could be useful for further research. Yet in order for humans to comprehend the embeddings we need to maps them either to 2D or 3D vectors and that is where dimensionaluty reduction algorithms are essential.

2.2.2.1 UMAP

Dimension reduction algorithms mostly form two main categories: ones are stronger preserving the pairwise distance globally - meaning try to preserve the structure amongst all the data samples; others prefer to save local distances. For example PCA [cite Hotelling] are assigned to the first caterogy, while t-SNE [cite Ulyanov] and Isomap are assinged to a latter one.

Uniform Manifold Approximation and Projection (UMAP) was build in a way to preserve both and it is a competitor of t-SNE approach, however is much faster and provides a transformation that can be used on the new data. UMAP is a graph-based algorithm and uses a k-nearest graph as a foundation. As any graph-based algorithm, its structure also includes two main steps:

- Graph construction procedure. During this stage a weighted k-neighbour graph will be constructed from the data. Specific transformation are applied on its edges to surround local distance. And the strong asymmetry common to k-neighbour graphs will be reduced.
- Graph layout building. In this stage one needs first to define an objective function that can preserve desired graph characteristics and then find a low dimensional representation of the graph that will minimize the objective.

In short, UMAP optimizes a low-dimensional graph from the high-dimensional one to be structurally very similar to each other. The algorithm has to important hyperparameters, which should be chosen carefully: *n_neightbors* and *min_dist*. The first one balances the local versus the global structure of the graphs, the higher the values the more finer details will be lost. The latter one controls how densly points will be located to one another.

Higher values of this parameter results in a loosier structure that preserves a broader topoly of the data.

2.2.2.2 PacMAP

Pairwise Controlled Manifold Approximation (PacMAP) is another dimensionality reduction method that is able to preserve both local and global data structure in a lower dimension space. Unlike other methods that regulate the stronger preservance of global structure by using more neightbors, PaCMAP uses mid-near pairs, to first capture global structure and then refine local structure, which both preserve global and local structure. It introduces a the following parameters: neighbor pairs (pair_neighbors), mid-near pair (pair_MN), and further pairs (pair_FP). [cite Yingfan] The neighbor pairs parameter is used during the building of the k-Nearest Neighbor graph. It is recommended to use the value around 10 for datasets with size smaller than 10000 [cite their repo]. The mid-near pair ratio parameter is the ratio of the number of mid-near pairs to the number of neighbors, whereas further pairs ratio is the the ratio of the number of further pairs to the number of neighbors. Configuring these parameters allow the user to achieve the desired ration between preserving local and global structure. Such method also works faster than UMAP, which allows to try out more hyperparameter options.

2.2.2.3 PCA

Principal component analysis (PCA) is an algorithm for linear dimensionality reduction [cite Pearson 1901]. PCA maximizes the variance in data's low-dimensional representation in order to keep as much information as possible. Essentially PCA gives projections $\tilde{x^{(i)}}$ for input samples $x^{(i)}$ that would be very similar to them, however have a much smaller dimensionality. Eigenvectors of the data covariance matrix are the directions of the most variance within the data, and the eignevalues correspoding to them are the amount of variance hidden in each dimension. That is why by projecting the data using the eigenvectors with the largest eingenvalues one will preserve the most varience of the data possible [cite MML-book].

The steps of PCA algorithm are the following:

- Subtract mean μ_d. To center the input data is not a nessesary step, but it is recommended to do so to avoid the numerical problems.
- Standartize the data. Calculate the standard deviation σ_d and standartize the data to have unit variance for every dimension.
- Do an eigendecomposition of the data covariance matrix. For that one first must compute the coveriance matrix itself, since the covariance matrix is symmetric from the spectral theorem one can always find an orthonomal basis of eigenvectors.
- Project the data. For that first standartize the point $x^* \in \mathbb{R}$ using μ_d and σ_d:

$$x_d^* \leftarrow \frac{x_d^* - \mu_d}{\sigma_d} \tag{20}$$

where $d = 1, ..., D$ and x_d^* is a d-th component of vector $x^* \in \mathbb{R}^D$ Get the projection as

$$\tilde{x^*} = BB^T x^* \tag{21}$$

with coordinates $z^* = B^T x^*$. Here B is a matrix of eigenvectors associated with the biggest eigenvalues of a covariance matrix.

[cite MML-book]

2.2.3 Clustering

After visualizing the embeddings, there is an interest in checking wether they form any kind of clusters, this question is discussed in the Section [TODO cite the section] using DBSCAN algorithm. Here will be provided the theory needed to understand how this algorithm works and how it can be set up.

2.2.3.1 DBSCAN

A density-based algorithm for discovering clusters (DBSCAN) does not require to provide the number of clusters in advance. Altough this is a nice quality of this algorithm it is not that important for current research. The goal of Section [cite Section] is to check wether different phenotypes form different clusters or for example wether corrupted images would fall into a separate clusters. In all cases the number of ground truth clusters is known in advance. However the fact that corrupted images form a more dense region in rather than non corrupted ones [cite Section] is an indicator that exactly DBSCAN would give a good clustering result.

This algorithm uses two hyperparameters = {eps, min_samples} to define the clusters. The first is the distance threshold, that is used to find determine wether a point is located in the neighborhood of the other point. The latter one is the minimum number of points that are needed to form one cluster. DBSCAN clusters points not only into several clusters but also determines the points that could not be assined to any cluster, which is also very useful in this research.

2.3 Imaging

2.3.1 Digital imaging

Digitally an image is represented as an array of size (H, W, C) where H is the height, W is the width C is the number of channels of the image. In this work $C = 1$ and $W = H$. A digitanlly represented image A then is the matrix:

$$A = \begin{bmatrix} a_{0,0} & \cdots & a_{0,W-1} \\ \vdots & \ddots & \vdots \\ a_{H,0} & \cdots & a_{H-1,W-1} \end{bmatrix} \tag{22}$$

where $a_{i,j} \in \mathbb{R}$. Both DIC and fluorescence images were provided in tag image file format (TIFF) format. For the processing convenience purpose all images were normalized to be in the range of $[0, 1]$:

$$a_{i,j}^{\text{norm}} = \frac{a_{i,j} - \min(A)}{\max(A) - \min(A)} \tag{23}$$

for $\forall i \in \{0, ..., W-1\}$ and $\forall j \in \{0, ..., H-1\}$

2.3.2 Microscopy imaging

2.3.2.1 Image acquisition peculiarities

Cells used in this research are growing in 96-well plates. A plate or a microplate in biology is a flat plate with multiple tubes ("wells"). The microscope used in the experiments takes photos of the well plate in random locations. The reason for that hides in the focusing settings of a microscope. To get a reasonably good not blurry photo a microscope has to focus on a specific location of the plate, the choice of this location however happens automatically, therefore the location of the focus is random (see Figure 3).

It might be problematic in the following sense: photos takes in such manner do not gurantee that the focus will land in distinct spots all the time. Meaning that some cells present in one of the photos might appear in the other ones as well. Since the photos are high-resolution they weil be first splitted into crops of size 256×256 each during the preprocessing. And it might happen that same cells might appear in several crops. That is why after the split of the image data between train, test and validation sets it might also happen that the same set of cells will once land in the train set and another time in the validation set, which will lead to a not completely fair and representative validaiton metrics during training.

In order to overcome this problem a much more expensive equipment is needed. Since in this case it doesn't bring too huge problems except for the fact that validation metrics might be lower than they should have been, there was no need to purchase a more expensive equipment.

2.3.2.2 Crops combination technique

Due to the restricted amount of memory on GPU deep learning models cannot have a high-resolution image as their input within current research. Yet this is also not obligatory: as the image contains dozens of cells within it, its processing can be limited to a crop of a smaller size. After the model has predicted fluorescence signal for each of the crops, output fluorescence images can be combined together to form a high-resolution image again. In this thesis the architecture of the model assumes an input of size $(256, 256)$ or

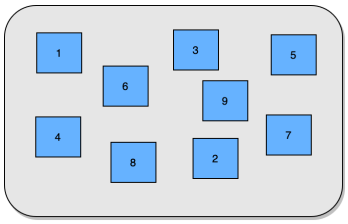

Figure 3: Way in which photos of the well-plate were taken

more specifically $(None, 1, 256, 256)$, where the first dimension is responsible for the batch size and the second one states that the input is a 1-channel image.

There are several ways of how one can split the image, the easiest approach would be to use a sliding window of size w. This algorithm is depicted in the Figure 4. A small window starts sliding the image from the left upper to the right down corner with step size s feeding the selected crops into a deep learning model. From the output of the model only a center part of such a crop is accepted to form a full fluorescence image. Border size b in this case is the size of the edges of the crop that are not accepted from the predictions of the deep learning model.

Having a desired border size, in order to accepted areas to be overlaped with each other without blank spaces, one has to adjust the step size to be:

$$s = w - 2 * b \tag{24}$$

When step size s is equal to window size w, there is no overlap between the windows.

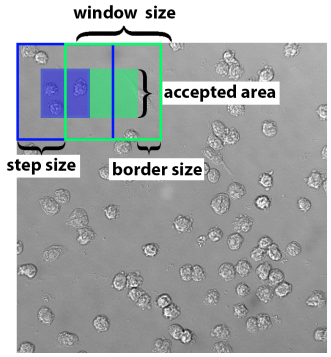

Figure 4: Sliding window approach for fluorescence prediction

The reason why not the full prediction is accepted to form the output hides in the following: trained models are less accurate on the borders of the crops rather than in the center. Most of the times there are cells on the borders of the crops that were sliced and therefore it might be impossible to make a good prediction for them just due to the lack of input information. Therefore the step size has to be smaller than the window size, so that the windows are overlapping and for each prediction we use only the image center and are allowed to ingore predictions on the border (see the comparison between different

border sizes in the Figure 5). This is dicsucced in more detail in Section [TODO reference the section]. Such approach helps to reduce the effect of the grid visible on the image composed of many small crops, which one can see in the Figure 5 on the left to almost non-visible borders as in the same Figure on right. This would of course take longer time in predictions, however as the speed is less crucial in comparison to the accuracy of the predictions.

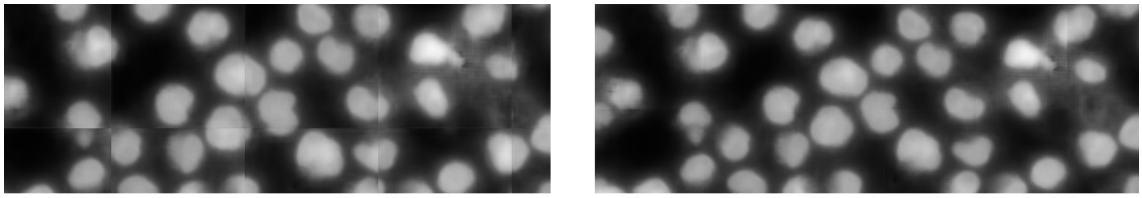

Figure 5: Difference of overlap between predictions on the resulting image

3 Implementation and experiments

In this chapter the results of all experiments performed for predicting fluorescence signal from 4 cell oganelles: nuclei, endoplaspic reticulum, Golgi apparatus, and full cell fluorescence are provided and discussed. It starts first with a description of the models and data used in the experiments, followed by 4 subsections dedicated to each of the organelles. Each subsection describes its own different approaches in, for example, pre- or postprocessing needed, difficulties that occured during preparation or training steps and well as results obtained for each organelle separately. At the end of this chapter an alternative way of the models performance estimation is provided, which is very important for the practical application of them.

3.1 Model training

3.1.1 Neural network architecture

As was described in section 2.2 the choice of the model architecture fell onto the UNet structure. Here will be provided a detailed decription of the architecture and the different layers used. An architecture used in this research was chosen based on paper [cite LaChance]. The input to this network is a 256×256-pixel DIC image that should be already preprocessed based on the corresponding to the desired organelle preprocessing pipeline. Specifications about different preprocessings are described separately in the next subsections dedicated to different organelles.

The encoder part of the UNet (Figure 6) step by step compresses spatial dimensions of the image (the spatial dimension size is detoned by a number on the left of each green block) into tensors or so-called feature maps with an increasing amount of filters (number of filters is denoted on the top of each green block). This allows to reduce the spatial information in the image and capture semantics. Decoder part on the contrary decompresses feature maps gradually increasing the amount of spatial information in tensors and reducing the number of filters. All convolutional layers use convolutions of size 3×3 with the corresponding number of filters. Downsampling in encoder reduces the spatial dimension twice during each step and implemented using max-pooling with a size of 2×2. Upsampling in decoder increases the spatial dimension also twice during each step and is implemented using transposed convolutions with a size of 2×2. After the first convolutional, that follows each max-pooling step, a batch normalization layer was used as it is well-known for speeding up the training process [cite Ioffe]. One should not forget though that using batch normalization might be sometimes dangerous due to the hidden information leaks it induces [cite Fetterman 2020]. Additionally dropouts were used for example for actin predictions as the model would encounter overfit quite easily there, however in the default architecture dropouts are not pressent. That is another thing that differs this architecture from the original one in [TODO Cite LaChance] paper. The last layer of the UNet here is a sigmoid activation function.

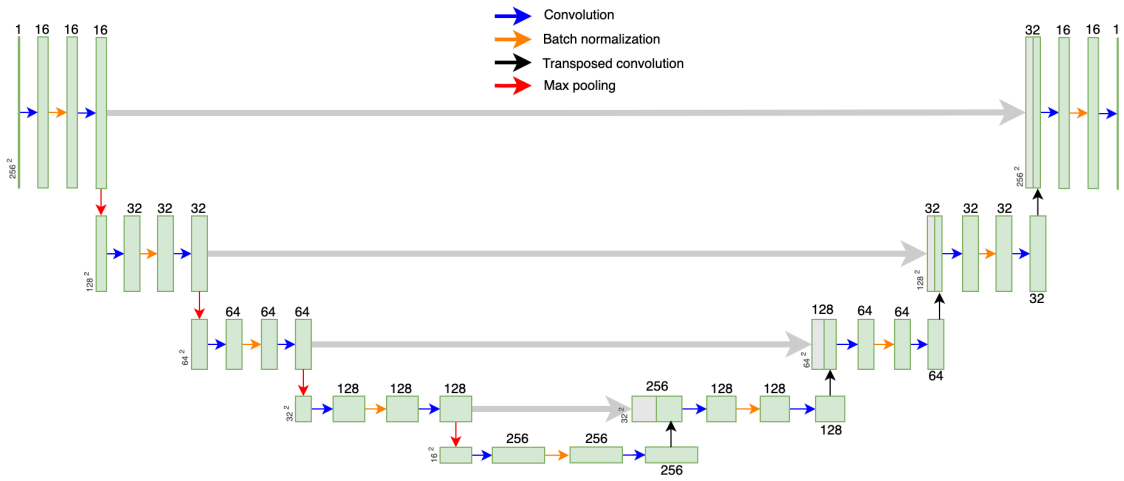

Figure 6: Unet

There is a space for potential improvements regarding the model architecture used in this research: for example, [Shiyui 2021] recommends to use special dense-block after each convolutional layer. They consist of another 3 convolutional layers with 24 filters, batch normalization layer and ReLU activations each. This could potentially facilitate efficient training of the model, still most probably the efficience comes mostly from Batch normalization layers that are already used in our architecture. Nethertheless the idea of using a bigger model such as one in [Shiyui 2021], or more specifically a model with more filters, indeed improves the predictions (shown in Section [TODO ref section]). That leaves the place available for further research and improvements regarding the size of the model and additional use of dense-blocks.

An interesting question that automatically rises here is what do UNet embeddings (output tensors from the encoder) represent. There is a big difference between any representation learning network such as an autoencoder and a UNet — a UNet model uses skip-connections that allow to propagate information between its encoder and a decoder. Meaning that embeddings do not contain purely semantic information, because essentially the network is not pushed towards compressing the information severely (as an autoencoder would do), but it should only extract relevant for segmentation features. One of the questions solved in this work was wether or not UNet embeddings are clustering based on the following classes: cell phenotypes, any kind of corruption within the data. For example, it would be bery usefull to be able to not only predict the data itselt, but also to say wether the prediction is reliable of not. The initial hypothesis here would be that if the predictions are not of a good enough quality this would be also reflected in the embeddings.

3.1.2 Available data

There were 4 targets studied in this research: nuclei, endoplaspic reticulum, Golgi apparatus and a full cell target. First 3 targets provide many insights on the state of cell based

on their quaintity, size and the intensity of fluorescence signal that they can produce by binding with the protein, the latter one is usefull in general for locating cells and calculating their area. There are of course other possible targets that could be used during the selection step of CLD, but the goal of this particular study was to provide the proof of concept on wether the network could potentially substitute manual fluorescence staining in general. The hypothesis on which we rely here is that if the model can successully predict fluorescence signal from some of the targets, then this research could be exended to other cell organelles as well.

The imaging data comes always in pairs (DIC + fluorescence imaging) and has the following structure:

```
dataset0
├── DIC
│   ├── {CHOZN, PHX, H19}_XY001.tif
│   ├── ...
│   └── {CHOZN, PHX, H19}_XY100.tif
└── {DAPI_nuclei, FITC, FITC_er, CY5_golgi}
    ├── {CHOZN, PHX, H19}_XY001.tif
    ├── ...
    └── {CHOZN, PHX, H19}_XY100.tif
...
datasetN
└── ...
```

Here a dataset$\{0, \ldots, N\}$ is one 96-well plane. There are only several datasets for each of organelle and each of them contains 100 images on random locations within this plate. Each dataset includes 2 subfolders — DIC and a fluorescence subfolder. The name of the latter one corresponds to the name of the fluorescent binding molecule as they are different for each target within the cell. Almost all plates contain pairs of images form one fluorescent staining target only. Each filename within the subfolder includes its index number between $\{1, \ldots, 100\}$ and the phenotype of the cell. "Cellular phenotype is the conglomerate of multiple cellular processes involving gene and protein expression that result in the elaboration of a cell's particular morphology and function" [TODO cite Jai-Yoon Sul 2009]. There are only 3 different phenotypes present across the datasets: CHOZN, PHX and H19. The latter however one is present only for full cell target.

Table 1: Available data for each fo the organelles

	Total images	Training crops	Validation crops	Test crops
Nuclei	595	$27,264$	$3,008$	$7,616$
Actin	400	$18,432$	$2,048$	$5,120$
Golgi	761	$23,036$	$2,336$	$6,347$
H19	400	$18,432$	$2,048$	$5,120$
Nucleolei	?	?	?	?

For the training all images are cropped into smaller crops of size 256×256 and split between training, test and validation sets with crops from one image being present in only one set. However it is still possible that the cells themselves might be mixed up between the sets, because the of the randomness of the microscopy focusing system (see

subsection 2.3.2.2). The summary of the total number of crops in each set is presened in Table 1.

3.1.3 Training costs estimation

For training purposes in this research cloud computing services were used, or more specifically - Amazon Web Services (AWS). These remotely located servers provide an possibility to train your models on a variety of graphic cards paying for a minute rate. In order to keep the costs unter the control it was important to estimate the time needed for training in advance to choose the most efficient GPU possible.

Cost estimation is additionally important for the model inference as well during the production. Although for production purposes the lambda functions from AWS can used. They can be triggered only when the inference request arrives and ca be turned off automatically shortly after.

For both training an inference purposes two GPU models were tested g3-4xlarge (NVIDIA Tesla M60) and p3-2xlarge (NVIDIA Tesla V100). The datasets on which the experiments were performed are the full cell target training and validation dataset. The resulting costs are presented in the Tables 2, 3.

Table 2: Costs estimations of AWS use for training models

	Runtime (1 epoch)	Dataset size	Costs per minute	Cost per epoch
g3.4xlarge	6.5min	$18,432$	0.07125$	0.3
p3.2xlarge	57sec	$18,432$	0.1911$	0.18

Table 3: Costs estimations of AWS use for inference purposes

	Runtime	Dataset size	Costs per minute	Cost of inference
g3.4xlarge	?mins	$2,048$	0.07125	?$
p3.2xlarge	?mins	$2,048$	0.1911	?$

In conclusion even though a p3 instance seems to be much more expensive, it is also much more efficient and the costs estimated to training times are significantly lower. That is why all the training experiments in this research were conducted on an NVIDIA Tesla V100 GPU.

3.1.4 Augmentations

Augmentations is a powerful regularization technique that helps the netwrk to generalize better [cite Wang 2017] and is an effective solution for a situation with the lack of labeled data [cite Yang 2022]. The main idea behind the augmentation is to increase the diversity of training data, when the acquisition of the real training data is expensive. Augmenting existing images creates the new synthetic samples which are hypotetically very close to the original true distribution of images. However one should be very cautios regarding the type of augmentations that can be used. Augmentation must enrich the dataset, however

should not change the semantics hidden in each image. The peculiarity of current research is the pair-wise correspondense between the DIC input and the output fluorescence. One should not change the input in such a way that the fluorescence signal could not be infered from it. Therefore the following augmentations have been used on cropped images:

- **Flipping**: Flip the crop horizontally (30% chance), vertically (30% chance) or both.
- **Random rotation**: Rotates the crop by a random angle.
- **Random scaling**: Reduces crop size by 100 (20% chance), 50 (20% chance) or 20 (60% chance) pixels from each side (down, top, left, right).
- **Contrast**: Descreases an image constrast in twice (50% chance), or triples it (50% chance). Applied with 20% chance.
- **Defocus blur**: Imitates a defocus blur of severity level 4 (see section [TODO cite section]) on an image with 20 % chance.

3.1.4.1 Special augmentations for rotation and scaling

Augmentations are chosed to be applied during training and the reason for that is to preserve the same conditions regarding the size of the datasets in order to have a fair comparison between approaches. For example, one decides to augment 20% of images and add them to an original dataset in order to expand it. Then the comparison between training with and without augmentations would be unfair as the sizes of the datasets are different, and it is not clear wether the performance improvement or decrease comes from the longer training (enlarged dataset) or augmentations.

Since augmentations are applied on crops directly during training there is a possibility to improve the rotation and scale of crops. The problem with this augmentations are depicted in the Figure 7 - after applying them there will appear a gray background, that wuold be filled with zeros in PyTorch implementation. However in since one has an original image where the crop has been cut out, one can easily restore background with original values and escape this problem alltogether.

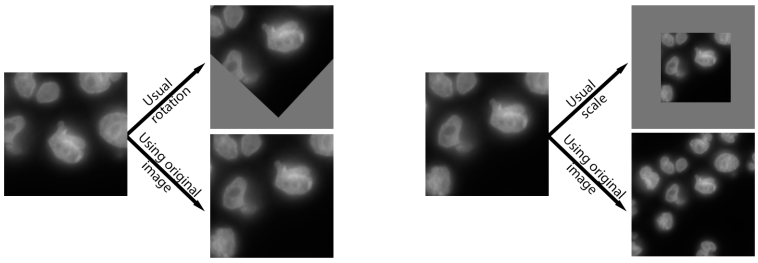

Figure 7: Using original image for rotation and scaling augmentations

Applying augmentations in combination with other regularization techniques has proven to be helpful against overfitting for the nuclei and ER training. Therefore it is recommened to use it in further research as well.

3.1.5 Model setup

3.1.5.1 Weight Initialization

These plots represent MSE

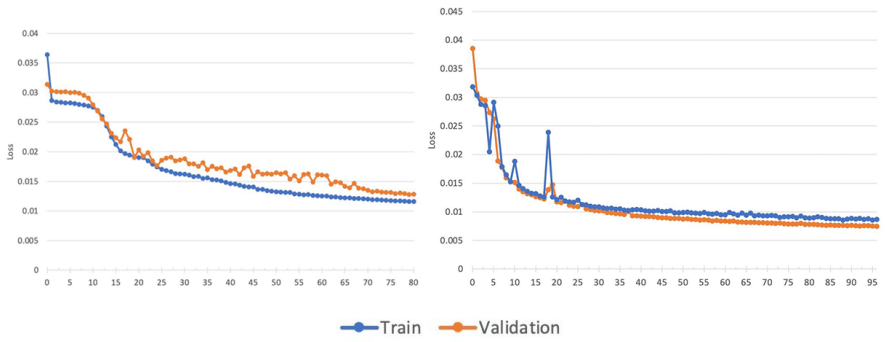

Figure 8: Nuclei training without and with custom weight initialization

3.1.5.2 Regularization

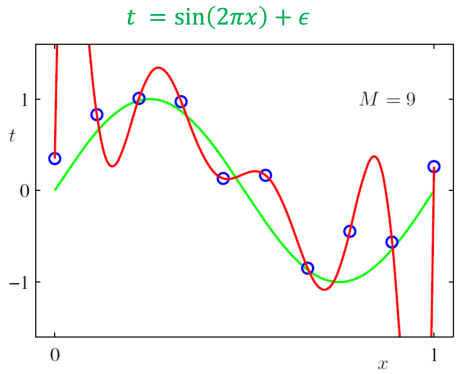

Figure 9: Overfitting

3.1.5.3 Optimizers

Comparison of different optimizers

3.2 Nuclei

3.2.1 Preprocessing

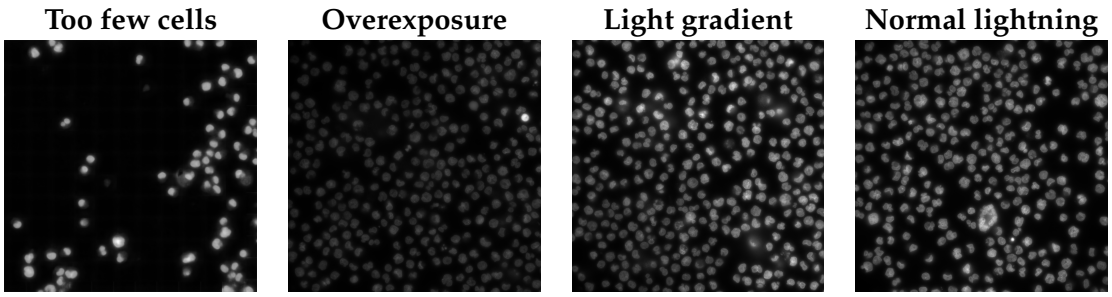

Figure 10: Different lightning conditions

3.2.1.1 Thresholding algorithms

Global and local thresholding

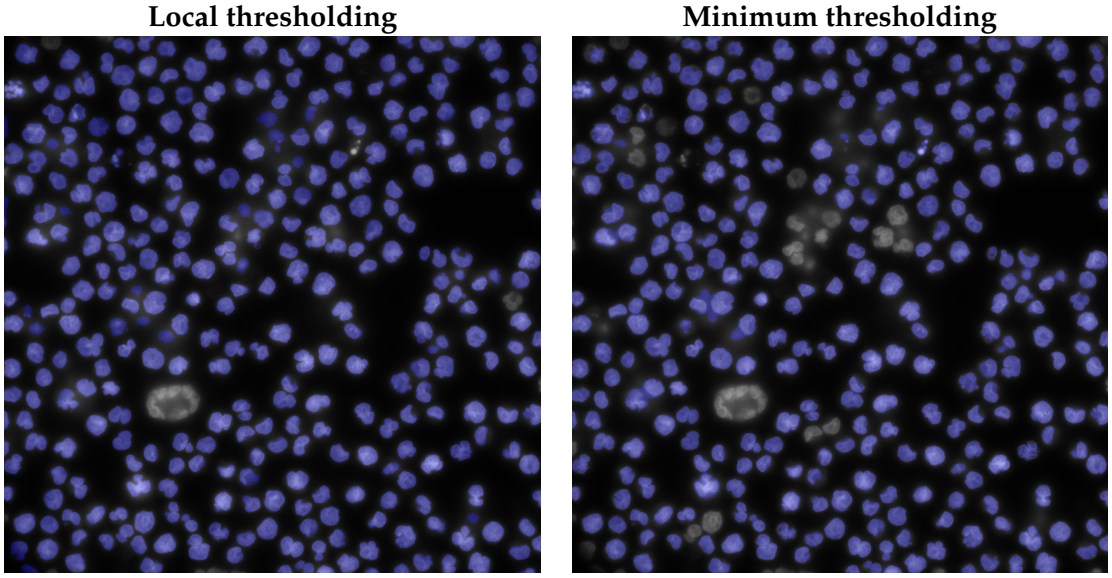

Figure 12: Local vs. Global thresholding (normal conditions)

3.2.2 Training and predictions

3.2.2.1 Convergence

Has the model converged or not. Will more data help?

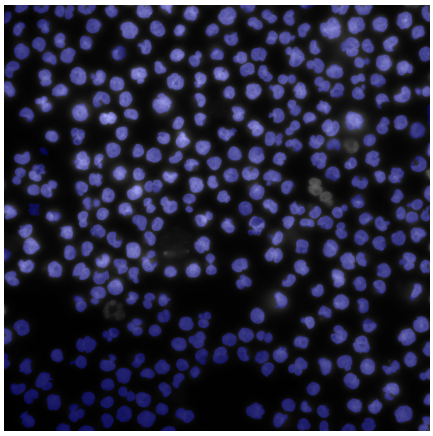

(a) Local

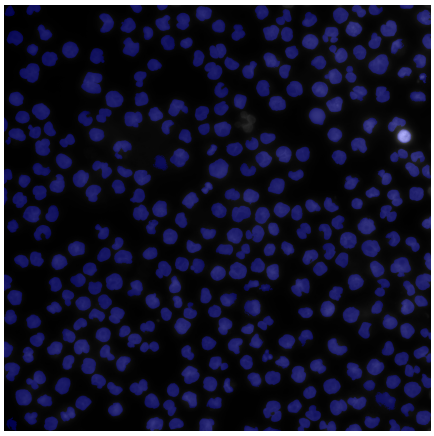

(b) Local

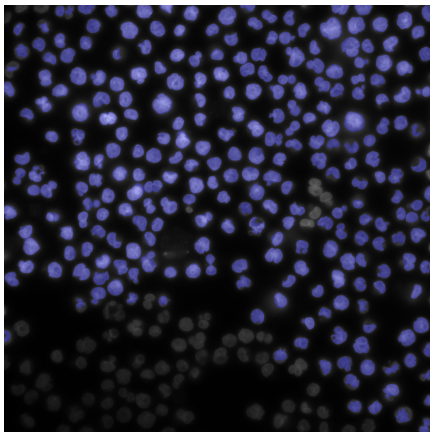

(c) Global, minimum

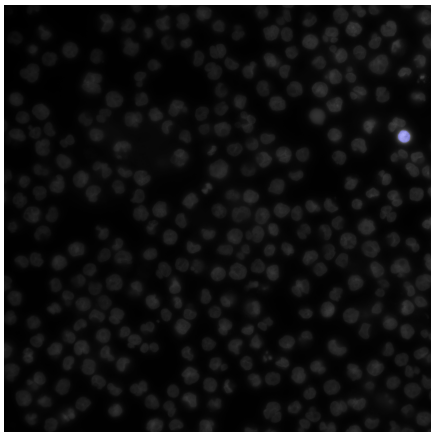

(d) Global, minimum

Figure 11: Local vs. Global thresholding

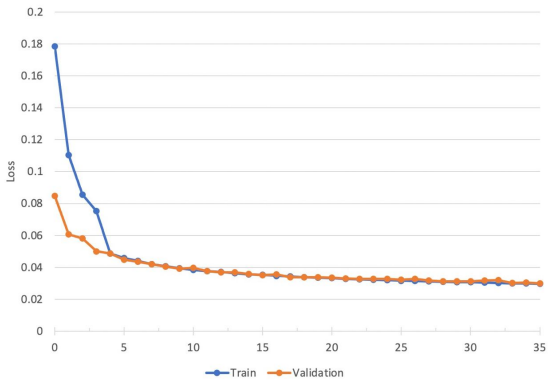

Figure 13: Having more data makes training more stable

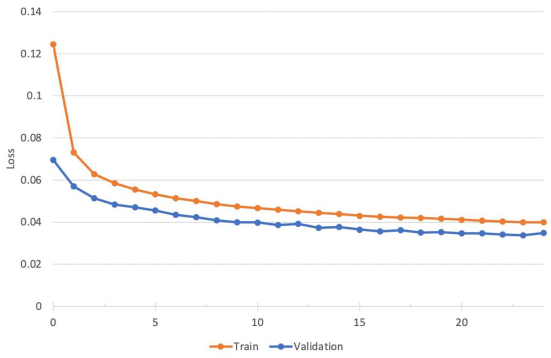

Figure 14: With regularization and augmentations PCC

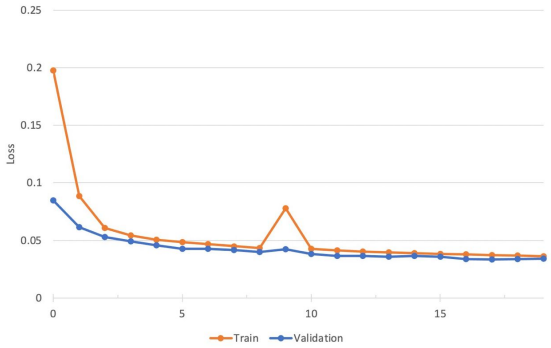

Figure 15: No regularization but augmentations

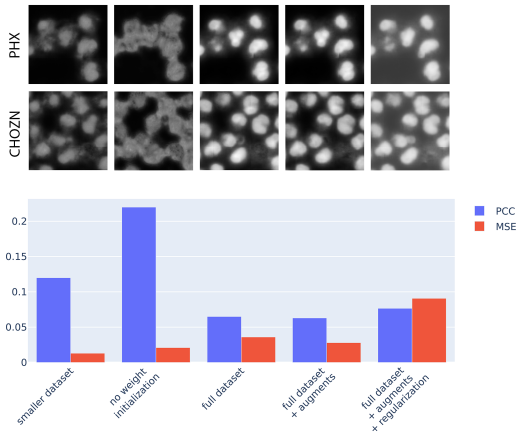

Figure 16: Difefrent models predictions and scores comparison

3.2.2.2 Predictions quality

Blurry, boundaries, not enough of details and possible improvements

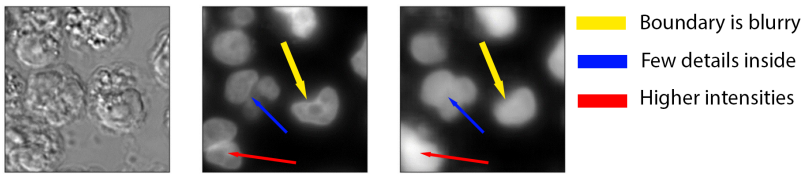

Figure 17: Problems in predictions

3.2.3 Postprocessing for nuclei segmentation

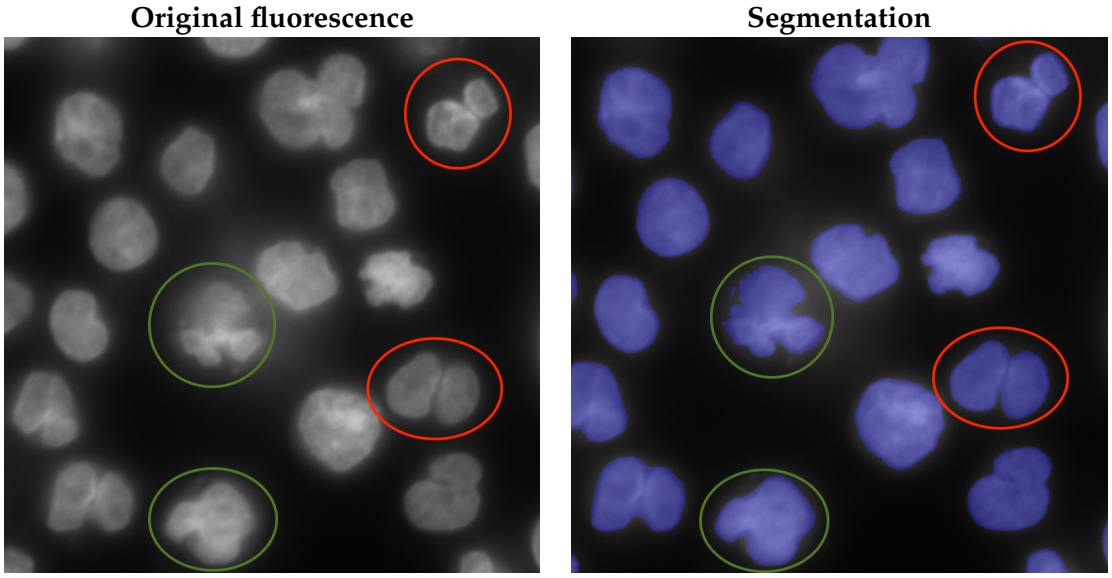

Figure 18: Closely located cells

Overall algorithm

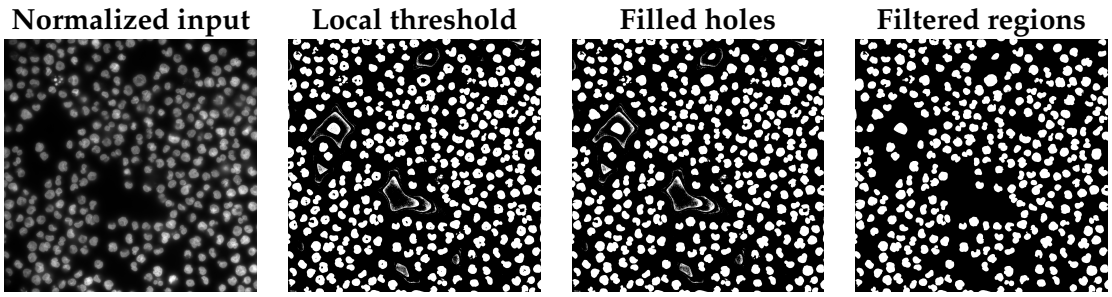

Figure 19: Fluorescence segmentation

3.2.4 Influence of scaling on predictions quality

Examples of predictions quality with different scales.

Table 4: Pearson correlation coefficients for downstream tasks for different scaling factors

	1.3 scale	0.7 scale	Train (1.0 scale + augments) Predict (1.3 scale)	Train (1.3 scale) Predict (1.0 scale)	Train (1.3 scale) Predict (0.7 scale)
Number of nuclei	0.987	0.995	0.975	0.971	?
Total intensity	0.902	.88	0.861	0.856	?
Mean intensity	0.922	0.906	0.88	0.872	?
Area	0.991	0.992	0.961	0.952	?

3.3 Endoplasmic Reticulum

3.3.1 Preprocessing

Algorithm 2 Fluorescence segmentation

1. Normalize image
2. Apply global *threshold_mean* to receive initial mask.
3. Zero out pixels outside the mask
4. Apply local thresholding.
5. Apply *fill_holes* transformation.
6. Morphological opening from OpenCV and Gaussian blur.
7. Run *findContours* from OpenCV in order to obtain separate regions and filter out too small regions.

Segmentation steps are also illustrated in Figure

Figure 20: ER prediction

3.3.2 Training and predictions

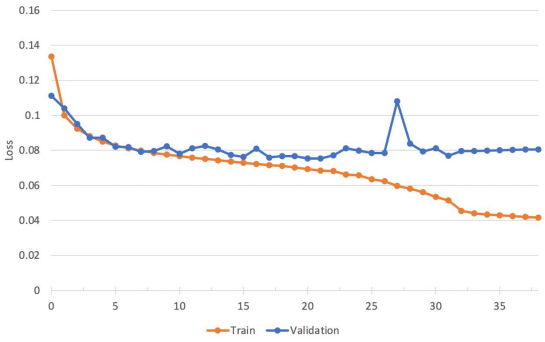

Figure 21: Overfit

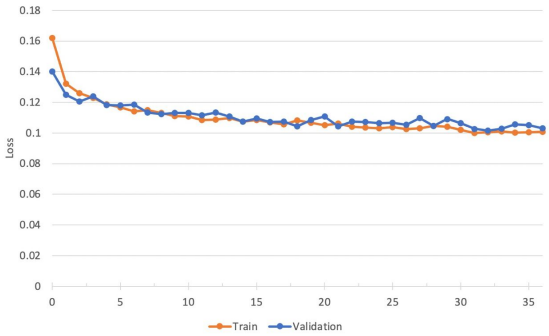

Figure 22: No overfit with augmentations

3.3.3 Combination of nuclei and actin predictions

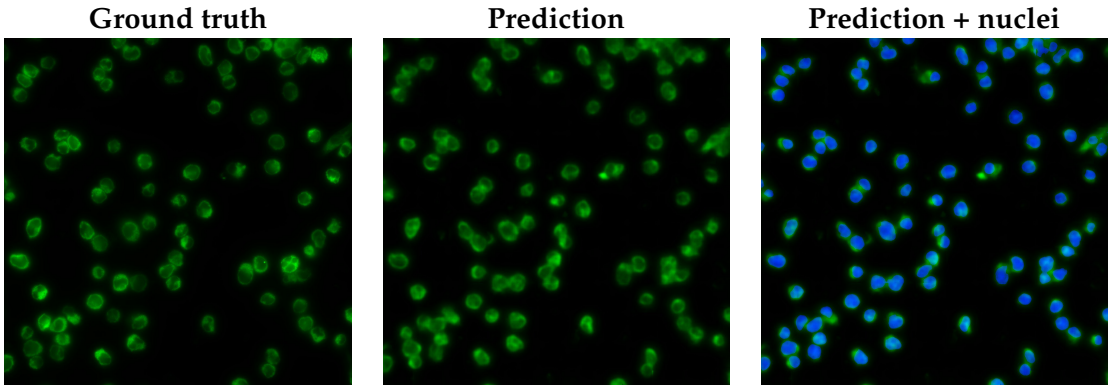

Figure 23: ER prediction

3.3.4 Generalizability across phenotypes

TODO train the model on one phenotype and predict on the other, compare predictions (visually?) postprocessing with metrics then? Add metrics

3.4 Golgi

3.4.1 Preprocessing

Enhancement

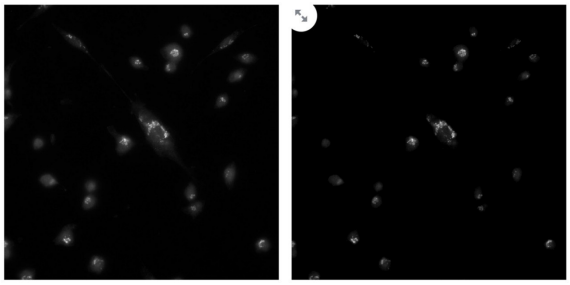

Figure 24: Golgi enhancement

3.4.1.1 Background removal algorithms

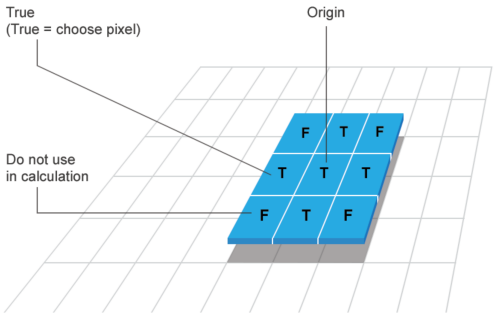

Figure 25: Structuring Element

Rolling ball algorithms

Rolling ball still leaves some noise

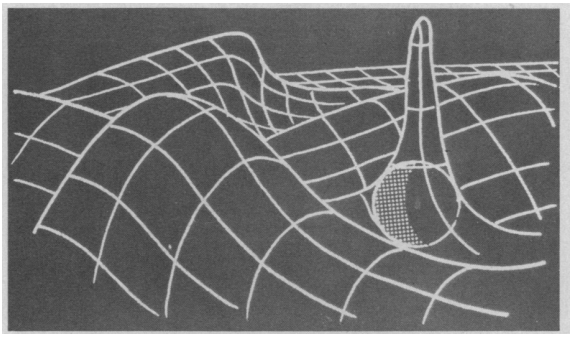

Figure 26: Rolling Ball

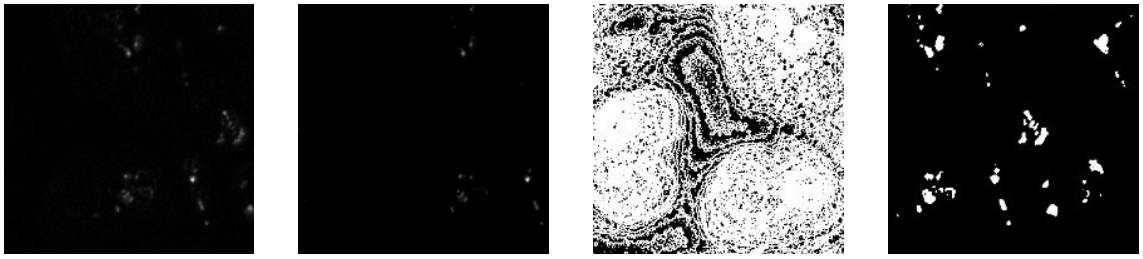

(a) (b) (c) (d)

Figure 27: (a) Vanilla pre-processing with automatic background removal algorithm only; (b) Additional clipping of lower intensities after vanilla pre-processing; (c) masked or subfigure (a); (d) mask of subfigure (b)

3.4.2 Training and predictions

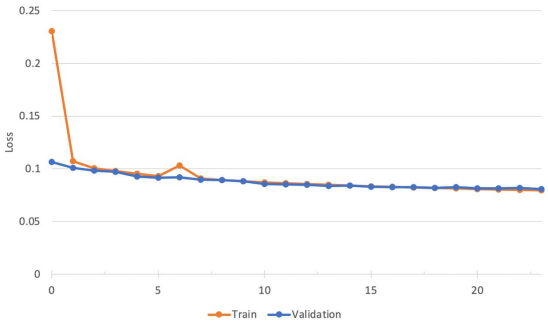

Figure 28: Straightforward training doesn't work

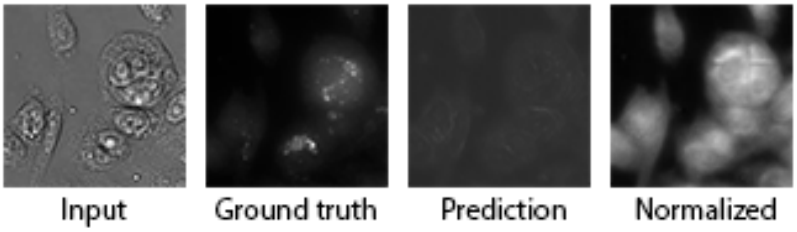

Figure 29: Training on original data

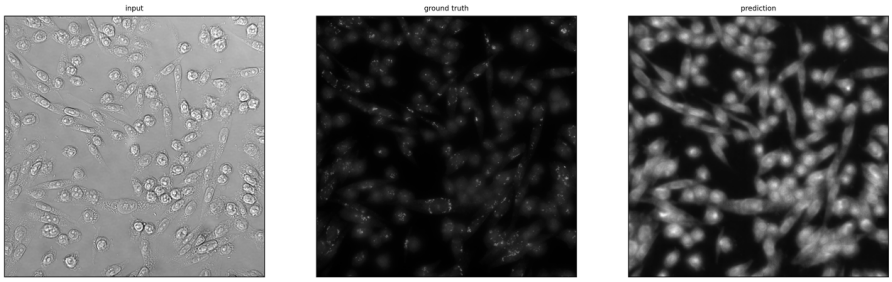

Figure 30: Full size predictions

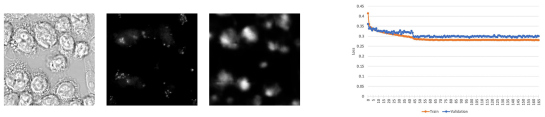

Figure 31: Training on the enhanced data

3.4.3 Alternative ways to improve predictions

3.4.3.1 Asymmetrical losses

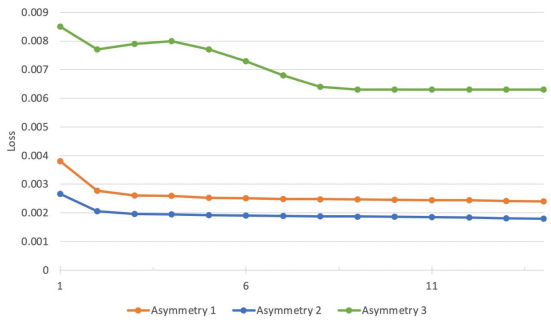

Figure 32: Asymmetrical training

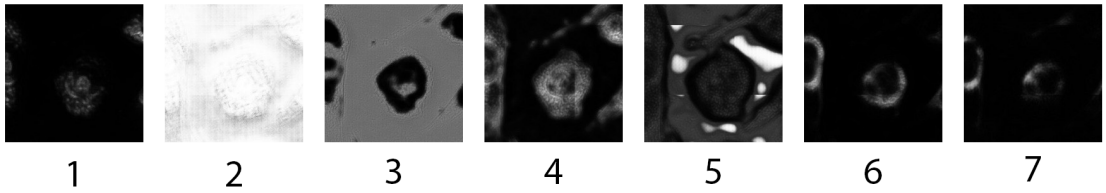

Figure 33: Asymmetrical training predictions

3.4.3.2 Use of gradient in loss

3.4.3.3 Noise reduction methods

3.5 GFP

3.5.1 Preprocessing

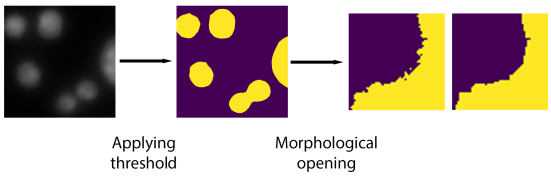

Figure 34: Converting GFP to a binary mask

3.5.2 Predictions

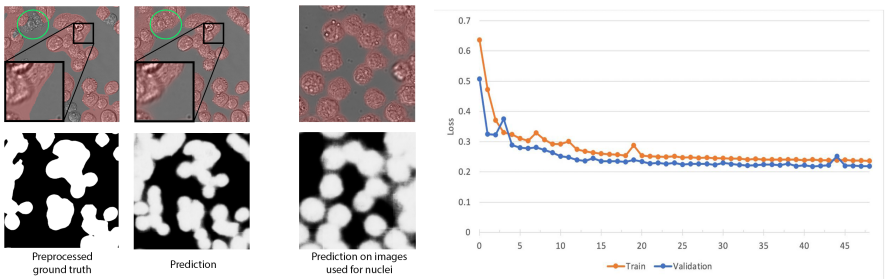

Figure 35: Training with BCE loss

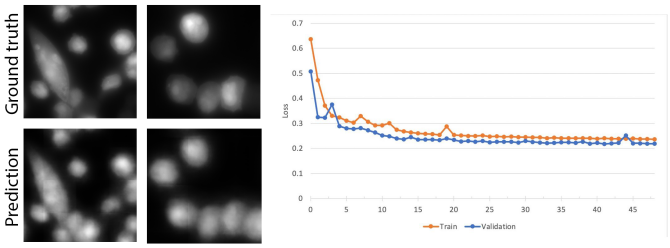

Figure 36: Training with Pearson correlation loss

Table 5: Correlation coefficients for downstream tasks

Binary training	Pearson	Spearman
Number of ER	0.67	0.64
Area	0.82	0.75
Continuos training	Pearson	Spearman
Number of ER	0.57	0.55
Area	0.26	0.64

3.5.3 Downstream metrics

TODO move to separate chapter?

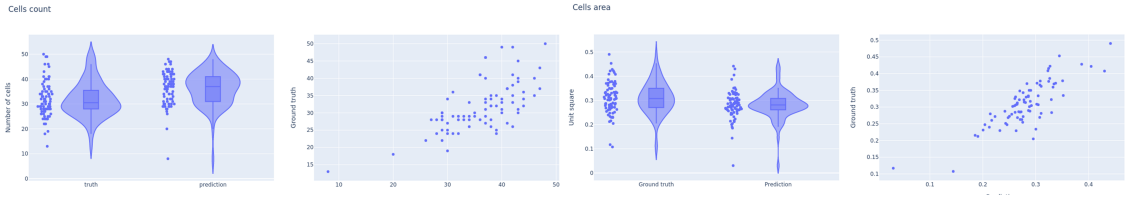

Figure 37: Downstream metrics

3.5.4 Combination of GFP, nuclei and ER

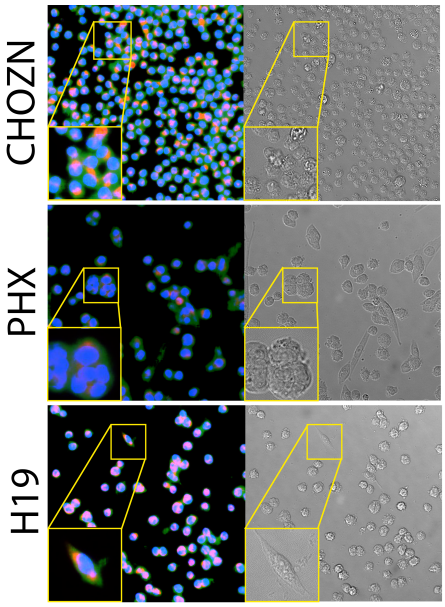

Figure 38: GFP, Nuclei and ER combined

3.6 Model evaluation

3.6.1 Metrics for downstream tasks

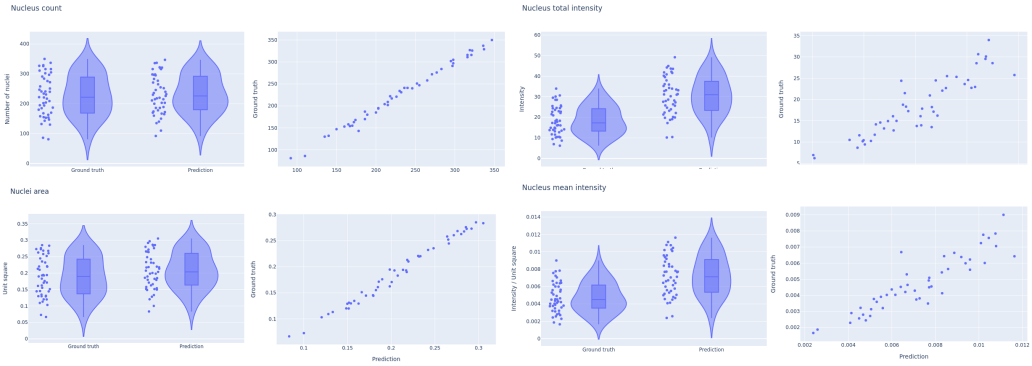

Figure 39: Metrics for downstream tasks on nuclei

Table 6: Correlation coefficients for downstream tasks on nuclei

	Pearson	Spearman
Number of nuclei	0.995	0.994
Total intensity	0.902	.911
Mean intensity	0.907	0.904
Area	0.992	0.990

3.6.2 Influence of different loss functions on metrics for downstream tasks

4 Stability study

4.1 Stability study

4.1.1 Artificial corruptions

Description of artificial corruptions.

Table 7: Hyperparameterization for different artificial corruption severities

Corruption \ Severity	-5	-4	-3	-2	-1	0	1	2	3	4	5
Defocus blur (radius)	-	-	-	-	-	0	0.5	1.0	1.5	2	3
Contrast (gain)	3.5	3.0	2.5	2.0	1.5	1	0.9	0.8	0.7	0.5	0.3
Brightness (bias)	-150	-135	-120	-90	-50	0	50	90	120	135	150

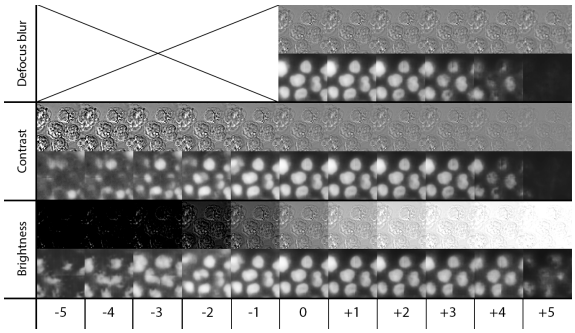

Figure 40: Influence of artificial corruptions on the predictions

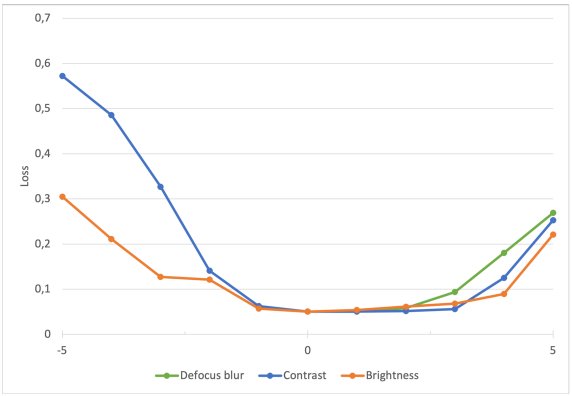

Figure 41: Change of Pearson correlation loss for artificial corruptions

4.1.2 Real corruptions

4.1.2.1 Not fixed cells imaging as corrupted input

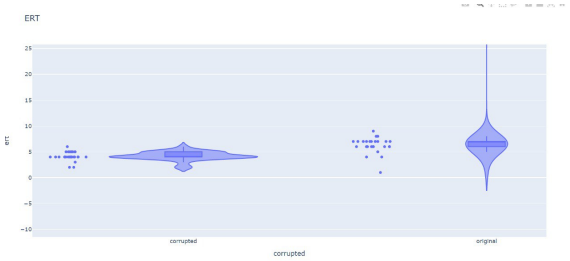

Figure 42: Online drift detection of not fixated cells

Scores of 0.91 however the threshold is 6, not corrupted data (fixed cells) mostly ert of 7 whereas corrupted data (not fixed cells) have an ert of 4. The threshold is therefore 6.

4.1.2.2 Real-world examples of corruptions

4.1.3 Influence of corruptions on metrics for downstream tasks

Calculate how metrics worsen when the evaluation stays the same, but the input is corrupted.

4.1.4 Improving predictions with additional corruption augmentations

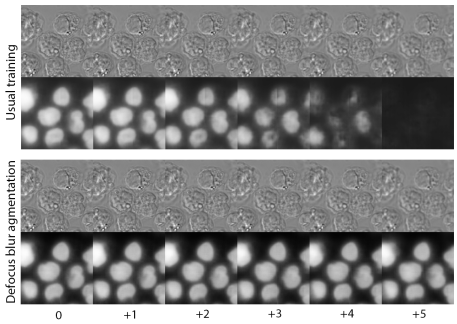

Figure 43: Using corruptions as augmentations improves predictions

4.2 UNET embeddings study

4.2.1 Application of various dimentionality reduction methods

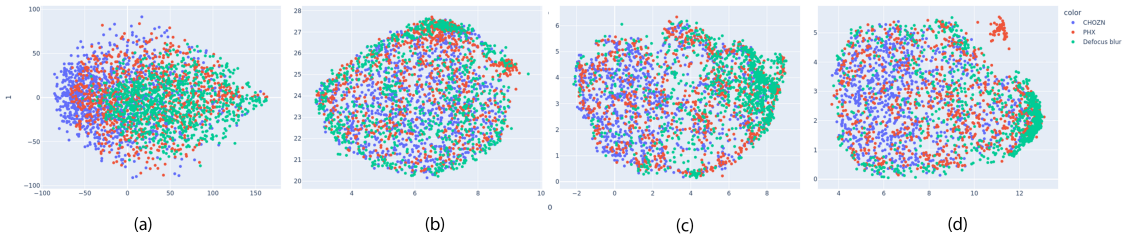

Figure 44: (a) PCA, (b) UMAP, (c) combination of PCA and UMAP with 10 and (d) 50 components

4.2.2 Autoencoder embeddings as an alternative

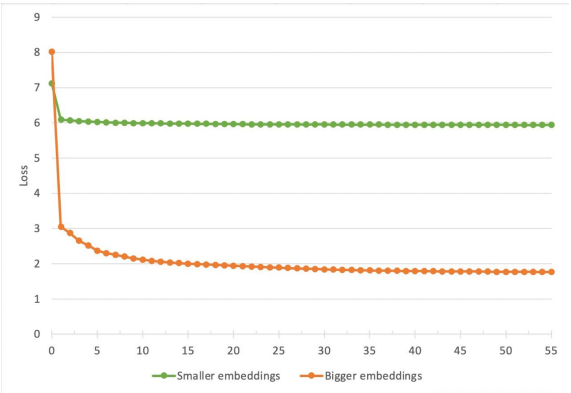

Figure 45: Autoencoders training convergence

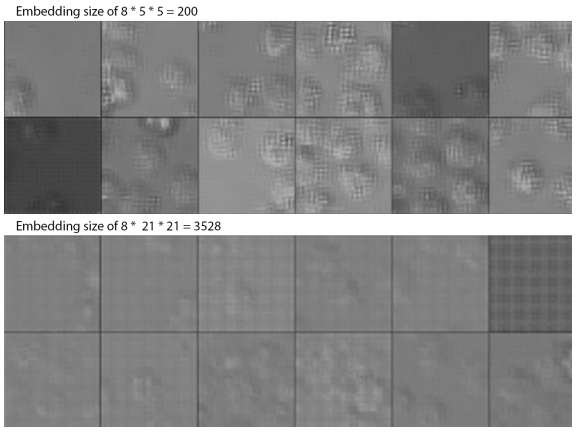

Figure 46: Samples drawn from the trained autoencoder

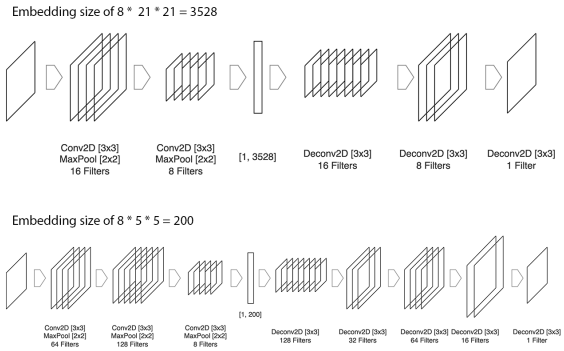

Figure 47: Architectures of two autoencoders

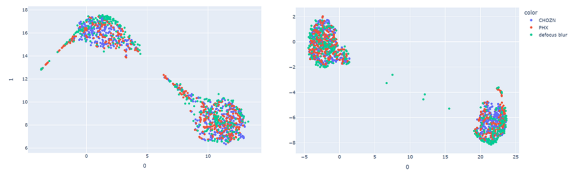

Figure 48: Autoencoder embeddings after applying PCA with 10 components and UMAP afterwards. Earlier epoch VS later epoch

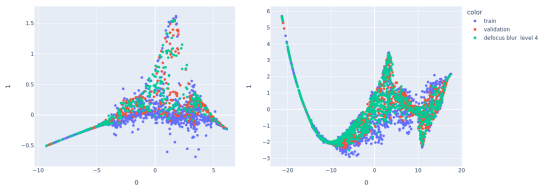

Figure 49: PacMAP does not provide information on the coruption

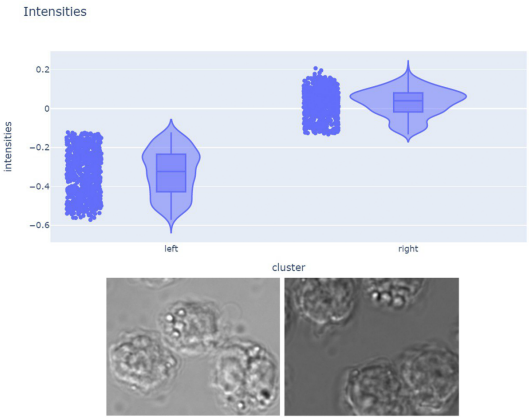

Figure 50: What do two UMAP clusters represent

4.2.3 Clustering of PacMAP embeddings

4.2.3.1 Clustering on UNet embeddings

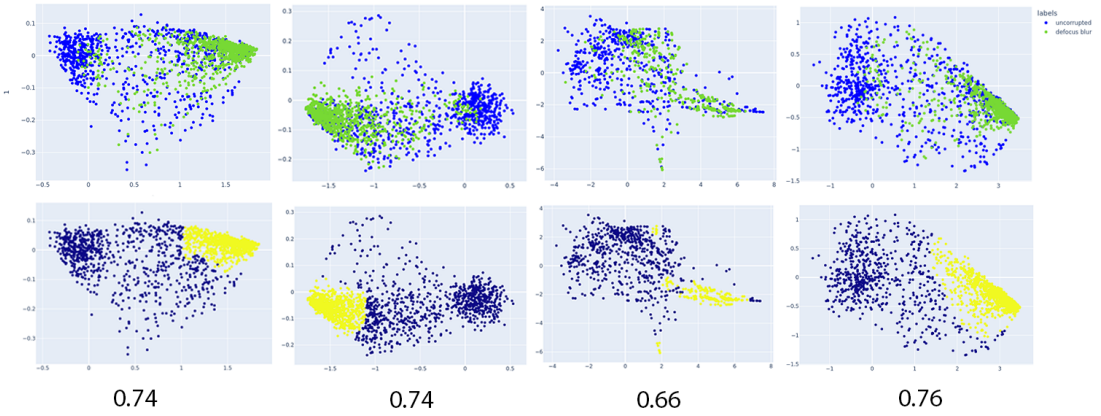

Figure 51: Clustering of UNet embeddings after PacMAP

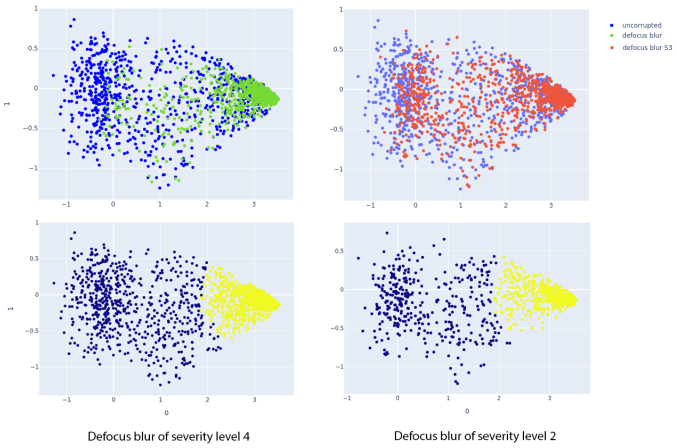

Figure 52: Clustering of UNet embeddings after PacMAP for different severities levels

TABLE with F1-score: 0.76 VS 0.64

4.3 Drift detection

4.3.1 A need to detect drift

4.3.2 Maximum mean discrepancy for drift detection

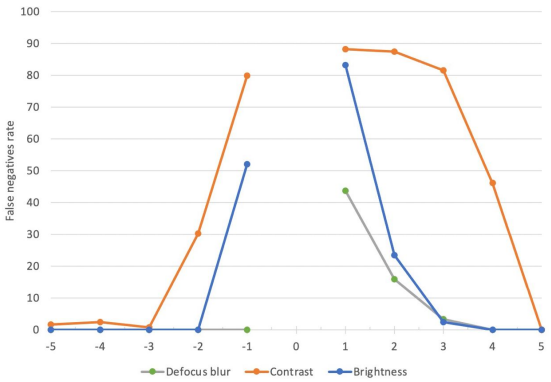

Figure 53: False negatives rate for drift detection on artificial corruptions

4.3.3 Online version of MMD algorithm

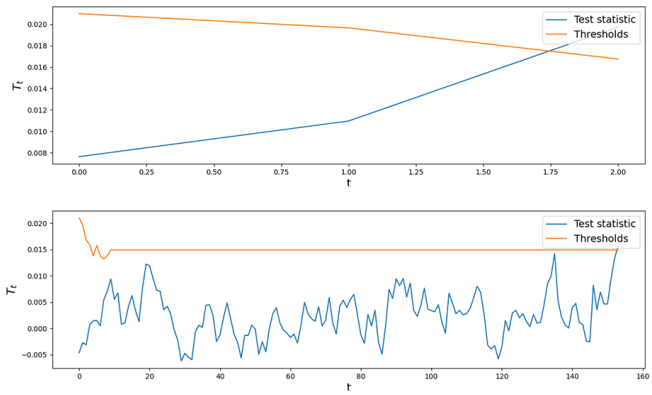

Figure 54: Expected runtime (ERT) for corrupted and in-distribution data

Table 8: Test window size influence on separability

W	2	5	10	15	20
Auc-Roc	0.85	0.92	0.98	0.90	0.88

Table 9: ERT influence on separability

W	32	64	128	256
Auc-Roc	0.90	0.95	0.98	0.98

Table 10: Severity of corruptions on separability

W	Level 2	Level 3	Level 4
Auc-Roc	0.84	0.92	0.98

Figure 55: AUC ROC scores for various defocus corruptions severities

5 Software Tools

5.1 Foundry. Palantir

5.2 AWS

5.3 Streamlit

6 Future research

" One limitation of our current work is that it is based on fixed cells that does not allow longitudinal imaging. This can be overcome by using fluorescent reporter cell lines or live cell dyes to provide the fluorescence ground truth (10) and enable dynamic observation. Another limitation of the DL framework we used here is that it cannot be generalized to different types of cells. Techniques based on transfer learning (https://doi.org/10.1038/s41551-019-0362-y, https://downloads.spj.sciencemag.org/bmef/2020/9647163.pdf) and domain adaptation (38) will be investigated in our future work to overcome this limitation."
TODO rephrase https://www.science.org/doi/10.1126/sciadv.abe0431

7 Summary

List of Figures

List of Tables